

LUMINOUS AND HIGH STELLAR MASS CANDIDATE GALAXIES AT $Z \approx 8$ DISCOVERED IN THE COSMIC ASSEMBLY NEAR-INFRARED DEEP EXTRAGALACTIC LEGACY SURVEY

HAOJING YAN¹, STEVEN L. FINKELSTEIN^{2,21}, KUANG-HAN HUANG³, RUSSELL E. RYAN⁴, HENRY C. FERGUSON⁴, ANTON M. KOEKEMOER⁴, NORMAN A. GROGIN⁴, MARK DICKINSON⁵, JEFFREY A. NEWMAN⁶, RACHEL S. SOMERVILLE⁷,
ROMEEL DAVÉ⁸, S. M. FABER⁹, CASEY PAPOVICH¹⁰, YICHENG GUO¹¹, MAURO GIAVALISCO¹¹, KYOUNG-SOO LEE¹²,
NAVEEN REDDY¹³, ASANTHA R. COORAY¹⁴, BRIAN D. SIANA¹³, NIMISH P. HATHI¹⁵, GIOVANNI G. FAZIO¹⁶, MATTHEW
ASHBY¹⁶, BENJAMIN J. WEINER¹⁷, RAY A. LUCAS⁴, AVISHAI DEKEL¹⁸, LAURA PENTERICCI¹⁹, CHRISTOPHER J.
CONSELICE²⁰, DALE D. KOCEVSKI⁹, KAMSON LAI⁹

Draft version July 13, 2018

ABSTRACT

One key goal of the *Hubble Space Telescope* Cosmic Assembly Near-Infrared Deep Extragalactic Legacy Survey is to track galaxy evolution back to $z \approx 8$. Its two-tiered “wide and deep” strategy bridges significant gaps in existing near-infrared surveys. Here we report on $z \approx 8$ galaxy candidates selected as F105W-band dropouts in one of its deep fields, which covers 50.1 arcmin² to 4 ks depth in each of three near-infrared bands in the Great Observatories Origins Deep Survey southern field. Two of our candidates have $J < 26.2$ mag, and are > 1 mag brighter than any previously known F105W-dropouts. We derive constraints on the bright-end of the rest-frame ultraviolet luminosity function of galaxies at $z \approx 8$, and show that the number density of such very bright objects is higher than expected from the previous Schechter luminosity function estimates at this redshift. Another two candidates are securely detected in *Spitzer* Infrared Array Camera images, which are the first such individual detections at $z \approx 8$. Their derived stellar masses are on the order of a few $\times 10^9 M_{\odot}$, from which we obtain the first measurement of the high-mass end of the galaxy stellar mass function at $z \approx 8$. The high number density of very luminous and very massive galaxies at $z \approx 8$, if real, could imply a large stellar-to-halo mass ratio and an efficient conversion of baryons to stars at such an early time.

Subject headings: cosmology: observations — galaxies: luminosity function, mass function

1. INTRODUCTION

In the recent years, deep near-infrared imaging surveys have begun to yield a significant number of candidate galaxies at very high redshifts. The wide-field surveys from the ground have produced a handful of bright candidates at $z \approx 7$ (e.g., Ouchi et al. 2009; Hickey et al. 2010; Castellano et al. 2010; Capak et al. 2011; Hsieh et al. 2012; Hathi et al. 2012), while the pencil-beam survey by the *Hubble Space Telescope* (HST) Wide Field Camera 3 (WFC3) within the historical Advanced Camera for Surveys (ACS) Hubble Ultra Deep Field (hereafter ACS-HUDF; Beckwith et al. 2006) and its two parallel fields (HUDF09; PI. Illingworth) have probed the fainter populations at $z \approx 7$ –8 (Oesch et al. 2010; Bouwens et al. 2010, B10; Bunker et al. 2010; McLure et al. 2010, M10; Yan et al. 2010, Y10; Finkelstein et al. 2010) and possibly out to $z \approx 10$ (Yan et al. 2010; Wyithe et al. 2011; Bouwens et al. 2011a). The WFC3 Early Release Science program (ERS, PI. O’Connell; Windhorst et al. 2011) has played an important role in connecting the “wide” and the “deep” ends of the exploration, allowing construction of $z \approx 7$ –8 samples at intermediate brightness levels (Wilkins et al. 2011; B11; Lorenzoni et al. 2011, L11). Meanwhile, the Hubble Infrared Pure Parallel Imaging Extragalactic Survey (HIPPIES; Yan et al. 2011) and the Brightest of Reionizing Galaxies

¹ Department of Physics & Astronomy, University of Missouri, Columbia, MO 65211, USA

² Department of Astronomy, The University of Texas at Austin, Austin, TX 78712, USA

³ Department of Physics & Astronomy, Johns Hopkins University, 3400 N. Charles Street, Baltimore, MD, USA, 21218

⁴ Space Telescope Science Institute, 3700 San Martin Drive, Baltimore, MD 21218, USA

⁵ National Optical Astronomy Observatory, 950 N. Cherry Ave., Tucson, AZ 85719, USA

⁶ Department of Physics and Astronomy, University of Pittsburgh, 3941 O’Hara Street, Pittsburgh, PA 15260, USA

⁷ Physics & Astronomy Department, Rutgers University, Piscataway, NJ 08854, USA

⁸ Astronomy Department, The University of Arizona, Tucson, AZ 85721, USA

⁹ University of California Observatories/Lick Observatory, University of California, Santa Cruz, CA 95064, USA

¹⁰ George P. and Cynthia Woods Mitchell Institute for Fundamental Physics and Astronomy, and Department of Physics and Astronomy, Texas A&M University, College Station, TX 77843-4242, USA

¹¹ Department of Astronomy, University of Massachusetts, Amherst, MA 01003, USA

¹² Department of Physics, Purdue University, 525 Northwestern Ave., West Lafayette, IN 47907, USA

¹³ Department of Physics & Astronomy, University of California, Riverside, CA 92521, USA

¹⁴ Department of Physics & Astronomy, University of California, Irvine, CA 92697

¹⁵ Observatories of the Carnegie Institution for Science, 813 Santa Barbara Street, Pasadena, CA 91101, USA

¹⁶ Harvard-Smithsonian Center for Astrophysics, 60 Garden Street, MS65, Cambridge, MA02138, USA

¹⁷ Steward Observatory, University of Arizona, 933 N. Cherry St., Tucson, AZ 85721, USA

¹⁸ Racah Institute of Physics, The Hebrew University of Jerusalem, Jerusalem 91904, Israel

¹⁹ INAF Osservatorio Astronomico di Roma, Via Frascati 33,00040 Monteporzio (RM), Italy

²⁰ Centre for Astronomy and Particle Theory, University of Nottingham, University Park, Nottingham, NG7 2RD, UK

²¹ Hubble Fellow

Survey (Trenti et al. 2011a) have been exploring the bright end of the population through a large number of random, discrete WFC3 pointings obtained during the *HST* parallel orbits. Surveys in foreground cluster fields utilizing gravitational lensing magnification have also resulted in a handful of promising candidates at $z \gtrsim 7$ –9 (e.g., Richard et al. 2006; Bradley et al. 2008, 2012; Laporte et al. 2011; Hall et al. 2012), which complement the surveys in blank-sky fields.

The Cosmic Assembly Near-Infrared Deep Extragalactic Legacy Survey (CANDELS; PIs: Faber & Ferguson; see Grogin et al. 2011 and Koekemoer et al. 2011) employs a two-tiered, “wide and deep” strategy, which makes it uniquely positioned in bridging the significant gaps among existing surveys. In particular, its “Deep” component will cover ~ 125 arcmin² in two fields upon completion, and its data will be ideally suited for studying galaxies at very high redshifts. In this paper, we report our preliminary results from the Deep observations in the Great Observatories Origins Deep Survey (GOODS; Giavalisco et al. 2004) southern field, where we use the nearly complete data set to study the galaxy population at $z \approx 8$. We use the following cosmological parameters throughout: $\Omega_M = 0.27$, $\Omega_\Lambda = 0.73$ and $H_0 = 71$ km s^{−1} Mpc^{−1}. The quoted magnitudes are all in the AB system.

2. DATA AND PHOTOMETRY

As detailed in Grogin et al. (2011), the CANDELS/Deep region in the GOODS-S field is located in its middle stripe where we have the deepest GOODS *Spitzer* coverage, which also includes the ACS-HUDF. The data used in this study include 100% of the observations in F105W (hereafter Y_{105}) and 83% of the observations in F125W (J_{125}) and F160W (H_{160}) scheduled for this field. The typical exposure times per sky position are 8090, 7450, and 7770 seconds in Y_{105} , J_{125} and H_{160} , respectively. Our present analysis is confined to the region where the effective integration times are at least 4000 seconds in all three WFC3 bands, which is 62.9 arcmin² in size. For the reason described below, we further exclude the region covered by the ACS-HUDF data, and the final effective area in our current study is 50.1 arcmin².

The products of the CANDELS data reduction (Koekemoer et al. 2011) include the science mosaics and the associated “root mean square” (RMS) maps. These RMS maps account for correlations between pixels that are introduced during the data reduction procedures (see e.g., Dickinson et al. 2004). Such correlations tend to reduce the measured pixel-to-pixel background noise in the *HST* images, and can lead photometry programs to underestimate the actual photometric uncertainties. We avoid this problem by computing uncertainties using the normalized RMS maps, summing their values in quadrature over the measurement apertures, and including an additional term for Poisson noise from the source flux (generally negligible for very faint dropout galaxies). The values of the CANDELS RMS maps have been validated both by comparison with autocorrelation measurements of the image noise, and by analysis of the dispersion of measurements in apertures randomly distributed within empty regions of the images. Our final mosaics have a pixel scale of 0″.06, and are tied to the same astrometric frame as the ACS data in GOODS.

The GOODS ACS data are used in our study to confirm the optical non-detections of the candidates (see §3.1). These data have been reprocessed to make mosaics at the same 0″.06 pixel scale for CANDELS. On average, the 5- σ sensitivities (as measured from the RMS maps) within a 0″.2-radius aperture in ACS F435W, F606W, F775W, F850LP (hereafter B_{435} , V_{606} , i_{775} , z_{850}) and WFC3 Y_{105} , J_{125} , and H_{160} are 28.04, 28.25, 27.65, 27.48, 28.15, 28.05, and 27.82 mag, respectively.

The HUDF region presents a complexity in our analysis. Both the HUDF09 WFC3 IR data and the ACS-HUDF data are much deeper than their counterparts that cover the rest (and much wider) area of interest. If we were to use these deeper data in our candidate selection, it would be very difficult to uniformly carry out the simulations that are necessary for the follow-up analysis (see §3.4). For simplicity, we therefore exclude the ACS-HUDF region from this current work.

In addition to the GOODS ACS data, we also have new ACS data in F814W (hereafter I_{814}) that CANDELS took in coordinated parallel mode to the WFC3 IR observations (see Grogin et al. 2011). These new ACS data suffer severely from the degraded charge transfer efficiency (CTE) of the aged CCDs, however, and the empirical correction of Anderson & Bedin (2010) were applied first before they were processed by the CANDELS reduction pipeline.

The photometry in WFC3 and ACS was done together by running the SExtractor software (Bertin & Arnouts 1996) in dual-image mode. We used the sum of the J_{125} and the H_{160} mosaics, each weighted by the inverse square of their RMS maps, as the detection image. A 3-pixel FWHM, 7×7 Gaussian filter was used to convolve the detection image, the threshold was set to 0.8- σ , and at least 4 connected pixels above this threshold are required. SExtractor provides a number of methods to measure flux, among which `MAG_APER`, `MAG_ISO` and `MAG_AUTO` are commonly used in dropout selections. `MAG_APER` magnitudes are calculated within a circular aperture of fixed size. As most high-redshift galaxies are compact, using these magnitudes can still be appropriate when the circular aperture size is carefully chosen so that it maximizes the S/N and minimizes the loss of light for the majority of the sources of interest. While it has the advantage of being robust in extracting very faint sources, `MAG_APER` has the disadvantage that real galaxies, which have different light profiles, have different fractions of light lost for a fixed aperture. `MAG_ISO` magnitudes are calculated within isophotal areas, which are set by the detection threshold and hence trace the different shapes of real galaxies. For this reason, `MAG_ISO` usually can be tuned to maximize S/N for galaxies of different morphologies. However, it does not capture the total light of a galaxy. `MAG_AUTO` magnitudes are calculated using adaptive elliptical apertures based on the first moment of the light distributions of galaxies (Kron 1980), and are the most suitable for deriving total magnitudes if an appropriate “Kron factor” is chosen. However, using a large Kron factor to capture total light usually means that the apertures are set too large for very faint sources such that their S/N are not optimized. Bearing both the advantages and the caveats in mind, we adopted the `MAG_AUTO` magnitudes (using the default [Kron factor, minimum radius]=[2.5, 3.5]) in this work.

Dropout selection uses hard boundaries in color space (see §3.1). As a result, photometric errors cause objects be scattered in and out of the selection area: an object whose intrinsic colors meet the selection threshold could be missed because of the errors in its measured colors, and vice versa. While this effect can be taken into account statistically by applying the correction for the “effective volume” (see §3.4), the candidate samples constructed using different photometry could differ significantly on an object-by-object basis. To demonstrate this effect, we also constructed a separate sample using **MAG_ISO** magnitudes, which is presented in the appendix and is compared to the **MAG_AUTO** sample. In both cases, we only kept the sources that have $S/N \geq 5.0$ in at least one band among J_{125} and H_{160} , measured within the **MAG_AUTO** or the **MAG_ISO** apertures.

We also make extensive use of the GOODS *Spitzer* IRAC data (Dickinson et al. 2004), which also have the same sky projection as other data here, and have a pixel scale of $0''.6$. We mostly concentrate on the 3.6 and $4.5 \mu\text{m}$ channels (hereafter [3.6] and [4.5]) in this study. We used a version of the GOODS photometry where the detection was done with a “mexhat” filter to optimize de-blending. We adopted **MAG_APER** within a $1''.5$ -radius (i.e., 2.5 pixels) aperture, and obtained the “total magnitudes” by applying the corrections as determined in the GOODS program where the aperture of this size has been used (e.g., Yan et al. 2005), which are -0.55 and -0.60 mag for [3.6] and [4.5], respectively.

3. Y_{105} -DROPOUT SELECTION OF CANDIDATE GALAXIES AT $Z \approx 8$

In this section, we describe our samples of candidate galaxies at $z \approx 8$ selected as Y_{105} -dropouts and the possible biases in our selections.

3.1. Color Criteria

Our first color criterion for Y_{105} -dropout selection is $Y_{105} - J_{125} > 0.80$ mag. This is the same as that employed by B10 and Y10, and is significantly larger than that of $Y_{105} - J_{125} > 0.45$ mag used in B11 and Oesch et al. (2012) where those authors have opted to included more galaxies at lower redshifts (starting at $z \gtrsim 7.2$) in their Y_{105} -dropout selection. Our larger color decrement threshold is sensitive to Lyman-break at $z \gtrsim 7.7$. When the objects have $S/N < 1$ in Y_{105} , we use their 2σ upper limits and only keep those that have $Y_{105} - J_{125} > 0.80$ mag as calculated using these conservative upper limits. Our second criterion is that a Y_{105} -dropout should have $S/N < 2$ in all four bands of GOODS ACS images ($B_{435}V_{606}i_{775}z_{850}$). This is to implement the invisibility requirement in these “veto” images, which is a necessary condition (though not sufficient) that the detected $Y_{105} - J_{125}$ color decrements in our candidates are not features in galaxies at low redshifts (for example, the 4000\AA break at $z \approx 2$) that could mimic the Lyman-break, because such low-redshift galaxies could have detectable fluxes in these bands. Setting the threshold to a quantitative value of $S/N < 2$ is somewhat arbitrary, however. Based on experience, adopting $S/N < 2$ for invisibility usually is a good compromise between minimizing the incompleteness and keeping the size of the initial candidate sample manageable for the later visual inspection

(see below). To exclude as much as possible the contamination from the red galaxy population at low redshifts, we impose a third criterion of $J_{125} - H_{160} \leq 0.3$ mag. This also largely limits our selection window to $z \lesssim 8.7$, and could be biased against genuine galaxies at $z \approx 8$ that have unusually large dust reddening or extraordinarily old stellar populations should they exist. Figure 1 shows our selection in the $Y_{105}J_{125}H_{160}$ space.

Each of these criteria introduces incompleteness, for which we will correct statistically (see §3.4).

3.2. Visual Inspection

The initial candidates have been visually inspected to ensure that they are legitimate sources in the IR images and that there is no reason to suspect that their photometry might be unreliable. Examples of problems that are not accounted for in the statistical noise model (and thus require visual inspection) include diffraction spikes, poorly rejected cosmic rays, inappropriate deblending, and bad background subtraction due to nearby neighbors. While such issues are rare in the entire photometric catalog, they can be selected when looking for objects with unusual colors, such as dropouts. Visual inspection step is necessary to reduce the rate of contamination, and is commonly adopted in dropout selections by various groups. It is somewhat subjective; different inspectors might not agree on a particular candidate, and even the same inspector might not be able to completely reproduce at different time his/her results on a large set of samples. Nevertheless, visual inspection is irreplaceable to get a reliable sample.

Ideally, the simulation discussed in §3.4 should also include this step when deriving the incompleteness correction. However, it is impractical to examine the 90,000 artificial galaxies inserted during the simulation. Nevertheless, we do not think that many of these would have been inappropriately rejected by visual inspectors, because the inserted galaxies do not resemble the artifacts or those with skewed photometry that we typically reject. Relative to the 90,000 inserted objects, we suspect only a handful would have these problems. Thus we do not think that the failure to visually inspect the artificial galaxies has a significant effect on our computation of the incompleteness and the effective volume.

In our visual inspection process, the initial candidates were first examined by one of us (HY) to get rid of the most obvious contaminants ($\gtrsim 300$ objects), such as image defects close to the field edges, diffraction spikes of bright stars, bad pixels, residuals of IR persistence, etc. The remaining candidates ($\lesssim 200$) were passed to six persons for independent inspections using a three-grade system of “firm acceptance”, “firm rejection” and “border-line case”. To be included in the final samples, a candidate should be firmly accepted by at least three inspectors, and should not be firmly rejected by more than one inspector. As described below, this approach has allowed us to study the possible systematic biases caused by visual inspections.

We note that the contemporaneous CANDELS I_{814} images have also been used in our current selection process. However, the flux upper limit estimate is subtle in these CTE-restored images when a source is undetected in single exposures, and a rigorous treatment to be adopted by our team is still yet to be finalized. To avoid possi-

ble changes to our sample in the future because of this reason, at this stage we refrain from directly using the I_{814} upper limits or S/N values in the quantitative veto process, and just use the I_{814} images in the visual inspection step (nevertheless, we do confirm that our current final candidates indeed formally satisfy the invisibility requirement in I_{814} ; see §3.3).

In addition to the usual examination of the mosaics, we have taken extra steps for assurance. In the IR, we have followed Yan et al. (2011) and examined the final candidates in their single-epoch WFC3 science images and the associated “data-quality” flags to confirm that they are not due to instrument defects. In the optical, we have constructed the “ χ^2 ” sum image of the four GOODS ACS $B_{435}V_{606}i_{775}z_{850}$ bands for our candidates. Based on Szalay et al. (1999), the χ^2 sum of these images optimally combines the signals from different bands and extend to a fainter limit that achieved by individual bands. The χ^2 images of our final candidates all have $\chi^2 < 3.73$, which is consistent with being drawn from a random sky distribution (Szalay et al. 1999) and thus further confirms their non-detections in the ACS.

3.3. Discussion of Sample

The final candidates in our sample are listed in Table 1. Their images are displayed in Figure 2.

3.3.1. “Negative Image” Test

To investigate the possible contamination of our sample by noise spikes due to background fluctuations, we carried out the so-called negative image test (e.g., Dickinson et al. 2004). The image mosaics described in §2, which all have zero mean background by construction (see Koekemoer et al. 2011), were multiplied by -1 to make any positive pixels to negative and vice versa. SExtractor was run in dual-image mode again on these negative images in the same way as in §2, using the weighted sum of the the negative J_{125} and H_{160} images as the detection image. After applying the same selection criteria for our Y_{105} -dropouts as in §3.1, only three “objects” survived, all of which have $J_{125} > 27.5$ mag, and all only show up in the negative J_{125} image. Their morphologies have odd shapes and are typical of noise spikes, and would be easily rejected during the visual inspection step. Therefore, we conclude that the contamination due to noise spikes is negligible in this work.

3.3.2. Interlopers

Our stringent requirements of non-detection in the ACS (individual bands and χ^2 sum) as well as $J_{125} - H_{160} \leq 0.3$ mag are effective in removing contaminations from red galaxies at intermediate redshifts (see Figure 1). In addition, the IRAC data for the isolated candidates support that they are unlikely contaminants of this kind, because such objects, if very weak in optical, should have very red colors at $1-4 \mu\text{m}$ such that $J_{125} - [3.6] \gtrsim 2$ mag (e.g., Yan et al. 2004). Our candidates that have IRAC flux measurements are all at $J_{125} - [3.6] \lesssim 1.3$ mag.

Another possible contaminant could be cool Galactic dwarf stars. Our criterion of $Y_{105} - J_{125} > 0.80$ mag is large enough to exclude most such contaminations. In addition, the number density of M/L/T-dwarfs in a high galactic latitude region such as the GOODS-S is likely

negligible (Ryan et al. 2011). Furthermore, our detailed morphological analysis in the accompanying paper (R. Ryan et al. 2012, ApJ submitted) shows that our brightest candidates are more consistent with extended light profiles than point-like.

Using the 4 Ms *Chandra* catalog of Xue et al. (2011), we find no X-ray counterparts to our candidates within $6''$. There is thus no evidence that these objects are AGN rather than normal galaxies.

3.3.3. Comparison to the Sample from Oesch et al. (2012)

Another paper based on the similar data set as ours was submitted by an independent group right after ours (Oesch et al. 2012, hereafter O12), and here we compare our sample to theirs based on the latest update available to us (P. Oesch, private communication, 2012).

In the overlapping region, the WFC3 IR data are essentially the same in both studies. However, O12’s reduction of the CANDELS WFC3 data is different from ours, and hence the end products of the science mosaics and the associated RMS maps are different. The photometry is also different. O12’s detection image is a χ^2 image derived from the J_{125} and H_{160} images, whereas ours is the weighted sum of the J_{125} and H_{160} . While they used MAG_AUTO as we also did, they adopted a smaller aperture (1.2 Kron) to compute colors. In addition, they stacked all the available ACS data in this region. We refrained from combining the late ACS data that suffer from the CTE problem with the earlier GOODS V2.0 $B_{435}V_{606}i_{775}z_{850}$ ACS data, and for the same reason we only used the I_{814} data in the visual inspection step (see §3.2). Finally, O12 adopted rather generous color criteria of $Y_{105} - J_{125} > 0.45$ mag and $J_{125} - H_{160} < 0.5$ mag, while we used $Y_{105} - J_{125} > 0.80$ mag and $J_{125} - H_{160} \leq 0.3$ mag.

All these factors contribute to the differences between the O12 sample and ours. It is interesting and instructive to compare the inclusion of the O12 candidates in our samples, and vice versa. Based on the photometry reported in O12, nine of their 14 Y_{105} -dropouts in the same field would be expected to enter our samples. Our sample, as shown in Table 1, include five of them. Among the four candidates not in our sample, three of them, CANDY-2209246371, 2432246169 and 2277945141 have $S/N < 5$ in J_{125} and H_{160} and are not included in our MAG_AUTO catalog, and the other one, CANDY-2272447364, has $Y_{105} - J_{125} = 0.18$ based on our photometry.

We note that one of our brightest candidates, AUTO_100, is not in the O12 sample. O12 believes that this object has a 2.4σ detection in I_{814} , derived in the conventional way using SExtractor. While our selection does not use the formal S/N estimates in I_{814} (see §3.2), we have also derived such estimates and confirmed after-the-fact that all our final candidates formally have $S/N < 2$. This particular object has $S/N < 2$ in both the MAG_AUTO and the MAG_ISO apertures (see also appendix). We attribute this discrepancy to the differences in photometry as outlined in §3.3.2.

To conclude, the level of overlap and discrepancy between these two samples is all well expected given the level of differences in their constructions. We further demonstrate this in the appendix.

3.4. Redshift Selection Functions

A given choice of Lyman-break color criteria, applied to a particular data set, leads to a probability distribution as a function of redshift and magnitude, $P(m, z)$ for selecting galaxies as dropout candidates. This probability distribution, in turn, corresponds to an effective volume (V_{eff}) for Lyman-break selection as a function of magnitude (Steidel et al. 1999). We have carried out extensive simulations to derive $P(m, z)$ and V_{eff} , in order to correct for the sample incompleteness that is inherent in the dropout technique. The results are the redshift selection functions at different brightness levels, which are shown in Figure 3.

To derive these functions, we put 90,000 artificial galaxies into the WFC3 and the ACS mosaics and calculated their rate of recovery $P(m, z)$ after applying the same color criteria as we did when constructing our dropout samples. These artificial galaxies have different fluxes and morphologies, with 70% being exponential disks and 30% having the de Vaucouleurs profile. Their sizes follow a log-normal distribution and $\theta(f) \propto f^{0.33}$, where θ is the peak size at flux f and is normalized to $0''.2$ at $H_{160} = 26$ mag. The input spectrum is from the models of Bruzual & Charlot (2003; BC03), and has a constant star formation history (SFH) and an age of 50 Myr. We adopted the extinction law of Calzetti (2001), and assumed that the distribution of $E(B-V)$ is a Gaussian function with mean $\langle E(B-V) \rangle = 0.1$ mag and scatter $\sigma = 0.1$ mag, restricted to $E(B-V) > 0$. The SEDs of the simulated galaxies were attenuated by the line-of-sight H I absorption according to the recipe of Meiksin (2006), which is very close to that of Madau (1995).

By calculating the ratio of the number of the recovered galaxies and that of the input ones, we obtained the selection function for the incompleteness correction. Figure 3 presents it as a function of J_{125} MAG_AUTO magnitudes, as these magnitudes are taken as the total magnitudes, and are the closest to the input total magnitudes of the simulated galaxies.

3.5. IRAC Counterparts

We have searched for IRAC counterparts of our Y_{105} -dropouts within $r = 0''.6$, and the results are also summarized in Table 1. Only two objects are securely detected in IRAC, namely, AUTO_035 and AUTO_293. As we will discuss later, their WFC3 versus IRAC colors are very consistent with being at high redshift. Objects AUTO_204, 212, 368 are in isolated regions, and they are invisible in the GOODS IRAC data. For all these objects, their $2\text{-}\sigma$ flux upper limits in [3.6] and [4.5] channels are calculated within a $r = 1''.5$ aperture.

All other objects in our samples are either blended with (denoted by “B” in Table 1) or severely contaminated (“C”) by foreground neighbors in IRAC and thus no useful information can be obtained.

3.6. Summary of Sample Limitations

Our sample suffer from the same kinds of incompleteness and contamination that are intrinsic to any dropout samples because of their selection technique. While a number of these issues have been mentioned in the above sections, we review them here before proceeding to discuss the statistical implications of our samples to astrophysical questions.

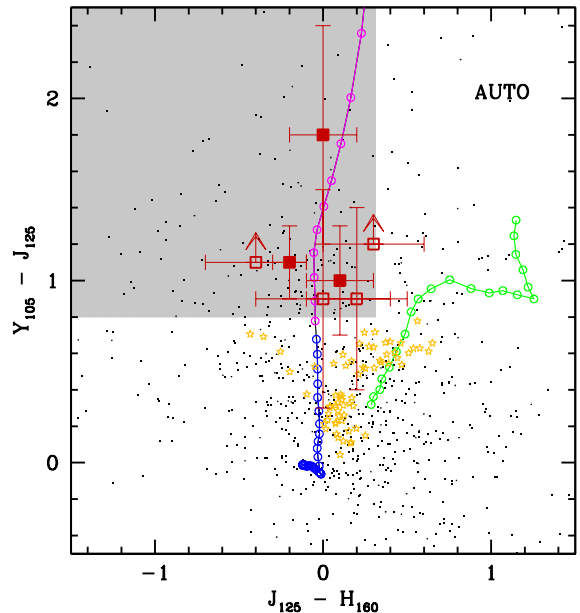


FIG. 1.— Selection of Y_{105} -dropouts in the $Y_{105}J_{125}H_{160}$ color-color diagram. The small dots are field objects that have $S/N < 2$ in ACS. The grey area is our selection region, where the brighter candidates ($J_{125} \leq 26.2$ mag) are plotted as red filled squares, and the fainter candidates as red open squares. The blue-magenta track shows a young galaxy (using a BC03 model of age 100 Myr and no dust extinction) at $z = 5\text{--}10$, with the blue section for $z < 7.7$ and the magenta section for $z \geq 7.7$. The orange stars show the colors of Galactic brown dwarfs (Leggett et al. 2002). The green symbols show the colors of a typical red galaxy at $z \approx 1\text{--}3$ simulated using a BC03 model ($\tau = 50$ Myr and age of 2.0 Gyr).

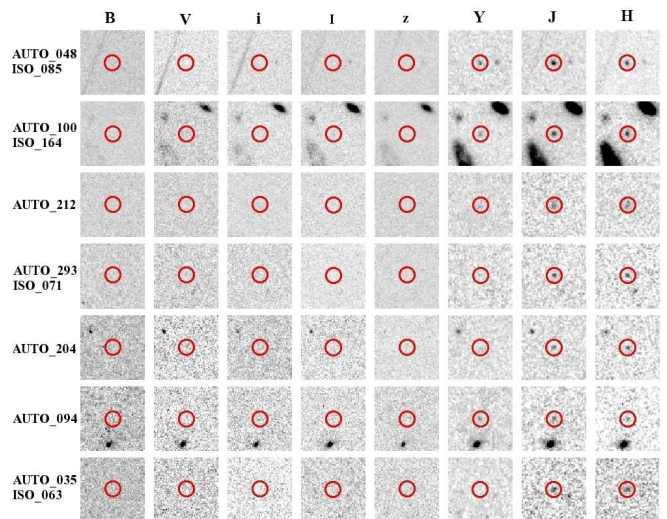


FIG. 2.— Images of the Y_{105} -dropouts in the AUTO sample, each $3''.1$ on a side. The locations of the candidates are at the center marked by red circles, which are $0''.5$ in radius. The common objects in the comparison ISO sample (see appendix) are also labeled.

There are two main factors that contribute to the incompleteness, which cause significant differences among samples as demonstrated in §3.3.1 and 3.3.2. First of all, an object whose intrinsic brightness is above our sensitivity limit could be undetected because its observed brightness could fall below the detection threshold due

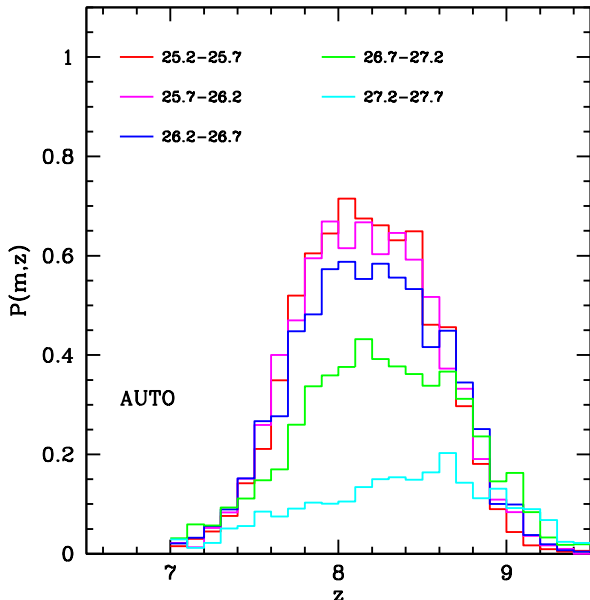


FIG. 3.— Redshift selection functions derived from simulations of our color selection in different magnitude ranges. The labeled magnitude ranges are based on `MAG_AUTO` in J_{125} .

to noise. Secondly, a genuine $z \approx 8$ galaxy that is detected in source extraction could still escape our color selection because it could be “scattered” out of the color selection region (see Figure 1) due to photometric error, or it could be incorrectly “vetoed” because of some unrelated events within its vicinity (for example, noise spikes) that accidentally increase its measured S/N in the veto images above the adopted quantitative veto threshold. Both effects have been taken into account by our simulations, and therefore can be corrected statistically.

The major factor that causes the contamination is the inclusion of low-redshift objects with spectral features that could mimic the Lyman-break at $z \approx 8$. Such contaminants could be selected because their $Y_{105} - J_{125}$ colors meet our color threshold, either intrinsically, or after being boosted by photometric error (i.e., being scattered into the selection region). Using the H_{160} data, our secondary $J_{125} - H_{160}$ criterion reduces the number of contaminants by rejecting those that have red SEDs. For other contaminants, the best way to reject them is to check their visibility in the veto images. As discussed earlier, the quantitative criterion of $S/N < 2$ gets rid of most of such objects, and the final step is the visual inspection. The caveat here is that we implicitly assume that the veto images are deep enough in detecting the contaminants in the blue bands, but this is not guaranteed. Currently we do not have a reliable way to assess this effect.

We point out that the rejection of contaminants based on their visibility in the veto images also introduces incompleteness, and that this happens both in the quantitative pre-screening (requiring $S/N < 2$) step and in the last visual inspection step. While the former can be statistically corrected by the simulations, the latter cannot.

4. DISCUSSION

Our samples are unique in two aspects. (1) We have two very bright candidates at $J_{125} \leq 26.0$ mag, which are at least ~ 1 mag brighter than the brightest Y_{105} -dropouts previously found. They are comparable in brightness to the brightest Y_{098} -dropouts reported by Yan et al. (2011) and Trenti et al. (2011a,b) in their WFC3 parallel surveys, but could be at higher redshifts because the redshift window of this current Y_{105} -dropout selection is higher than that of the existing Y_{098} -dropouts. (2) Two other Y_{105} -dropouts, which are not among the brightest in the WFC3 bands, are securely detected in IRAC, which is in sharp contrast to previous results where only non-detection in IRAC have been reported for Y_{105} -dropouts. Here we discuss the implications of both.

4.1. Stellar Population and Stellar Mass

We investigate the stellar populations of the IRAC-detected Y_{105} -dropouts, `AUTO_035` and `AUTO_293`, by analyzing their spectral energy distributions (SED) through template fitting. The approach here is similar to that of Finkelstein et al. (2011). We first use the EAZY code (Brammer et al. 2008) and the photometry of the GOODS ACS & CANDELS WFC3 data to estimate photometric redshifts (z_{phot}). The full SED (including the IRAC photometry) is then fitted to a suite of templates based on the updated models of BC03 (the so-called “CB07” models). A Salpeter initial mass function (Salpeter 1955) and the metallicities of $0.02-1Z_{\odot}$ are adopted. The templates have a range of exponentially decreasing and increasing SFHs (see also Papovich et al. 2011), and can include nebular lines based on the number of ionizing photons and metallicity of a given model (B. Salmon et al. in preparation). We assume the extinction law of Calzetti (2001) with $E(B - V) = 0-0.5$ mag and the H I absorption as formulated in Madau (1995). The results are summarized in Figure 4. We note that fitting redshift and other properties simultaneously does not significantly change these results, and the differences are captured in the errors that we quote here.

The best-fit photometric redshifts are $8.5^{+0.2}_{-0.5}$ and $8.9^{+0.2}_{-0.5}$ for `AUTO_035` and `293`, respectively, which are consistent with the redshift window of our color selection. Adding the formal I_{814} limit to the fitting process does not change the results. We fit the SEDs with and without the contribution from nebular lines, and both results suggest high stellar mass (\mathcal{M}_{*}) in the range of 10^9 to $10^{10} M_{\odot}$ for both objects. Including nebular emission lines, we obtain $2.5^{+4.7}_{-1.4} \times 10^9$ and $0.9^{+3.0}_{-0.1} \times 10^9 M_{\odot}$ for `AUTO_035` and `293` respectively, while without nebular emission lines these are $10.5^{+1.8}_{-8.1} \times 10^9$ and $2.6^{+1.8}_{-1.4} \times 10^9 M_{\odot}$, respectively. The error bars reflect the 68% confidence level of the fit. Labbé et al. (2010a) derived the stellar masses of galaxies at lower redshifts of $z \approx 7$ using models without nebular emission, and the average value is $\sim 10^9 M_{\odot}$. The two objects in our sample have comparable or even larger values using similar models, which are surprisingly high at such an early epoch.

Using the \mathcal{M}_{*} estimates, we obtain the first measurement of the mass function (MF) of galaxies at $z \approx 8$ at the high-mass end. As we only have two objects whose \mathcal{M}_{*} values are reasonably similar, we opt to

count them within one mass bin of a ± 0.4 dex bin size. The two different sets of models result in significantly different mass estimates, and therefore the bin center is different for each case. Assuming a top-hat selection function of our survey within $7.7 \leq z \leq 8.7$, we get $\phi(\log \frac{M_*}{M_\odot})|_{9.2 \pm 0.4} = (1.9^{+2.4}_{-0.6}) \times 10^{-5} \text{ Mpc}^{-3} \text{ dex}^{-1}$ if we adopt the values derived using the models with nebular emission. If we apply the effective volume (V_{eff}) correction of the survey instead (see §3.4), we obtain $(3.1^{+4.0}_{-1.0}) \times 10^{-5} \text{ Mpc}^{-3} \text{ dex}^{-1}$. Here we use $V_{eff} = \int V_{eff}(m_J) dm_J = \int \int dm_J dz P(m_J, z) dV/dz$, where dV/dz is the unit co-moving volume at redshift z , and $P(m_J, z)$ is the redshift selection function at different magnitudes m_J as derived through simulations (see Figure 3). The error bars here reflect the 68% interval of the uncertainties caused by the Poisson noise in the sample. For the case of using the \mathcal{M}_* estimates based on the models without nebular lines, all the above values are applicable at $\phi(\log \frac{M_*}{M_\odot})|_{9.7 \pm 0.4}$.

The contribution of these objects to the global stellar mass density, ρ_* , at $z \approx 8$ within our survey volume is $(3.3^{+7.4}_{-1.4}) \times 10^4$ and $(12.6^{+3.4}_{-9.0}) \times 10^4 M_\odot \text{ Mpc}^{-3}$ based on the models with and without nebular emission lines, respectively, if assuming a top-hat selection function at $7.7 \leq z \leq 8.7$. The errors reflect the 68% confidence level of the fitting results. If we apply the same correction for V_{eff} as above, we obtain $\rho_* = (5.5^{+12.6}_{-2.4}) \times 10^4$ and $(21.2^{+5.8}_{-15.3}) \times 10^4 M_\odot \text{ Mpc}^{-3}$.

We derive the mass-to-light ratio of these two objects using their $4.5 \mu\text{m}$ flux as a proxy to L_V . Using the fit results with contribution from nebular lines, we obtain $\mathcal{M}_*/L_V = 0.07^{+0.14}_{-0.04}$ and $0.04^{+0.13}_{-0.00}$ for AUTO_035 and 293, respectively. Without the contribution from nebular lines, we obtain $\mathcal{M}_*/L_V = 0.31^{+0.06}_{-0.24}$ and $0.12^{+0.08}_{-0.06}$. The latter values are in general agreement with those obtained by Labbé et al. (2010a,b) through stacking analysis of the IRAC data of the Y_{098} -dropouts and the Y_{105} -dropouts in the WFC3 ERS field (see also González et al. 2011) and the HUDF using similar models without nebular lines. On the other hand, Labbé et al. (2010b) estimated that nebular lines have a small impact on \mathcal{M}_*/L_V , reducing it by ~ 0.2 dex. Our results suggest a stronger effect, reducing \mathcal{M}_*/L_V by ~ 0.5 – 0.6 dex.

4.2. Constraint on the LF

Here we use our sample to constrain the LF at $z \approx 8$. We adopt the $J_{125} \text{ MAG_AUTO}$ values of the candidates as their total magnitudes.

After applying the correction for V_{eff} , we obtain the stepwise LF in the five 0.5-mag bins (25.45, 25.95, 26.45, 26.95, 27.45) mag as $\phi = (2.5^{+5.8}_{-0.6}, 2.5^{+5.8}_{-0.6}, 2.8^{+6.3}_{-0.6}, 3.6^{+8.3}_{-0.8}, 24.2^{+22.6}_{-5.6}) \times 10^{-5} \text{ Mpc}^{-3} \text{ mag}^{-1}$. These number densities are shown in Figure 5, and compared to the predictions from a number of Schechter LF estimates at $z \approx 8$ (M10; Y10; B11; L11). The black squares are our observed densities, while the red squares are the densities after correcting for V_{eff} . The error bars represent a Bayesian 68% credible interval, indicating the central 68 percentile range for the posterior distribution of the true number density assuming Poisson statistics. These uncertainties account for the incompleteness, but do not account for

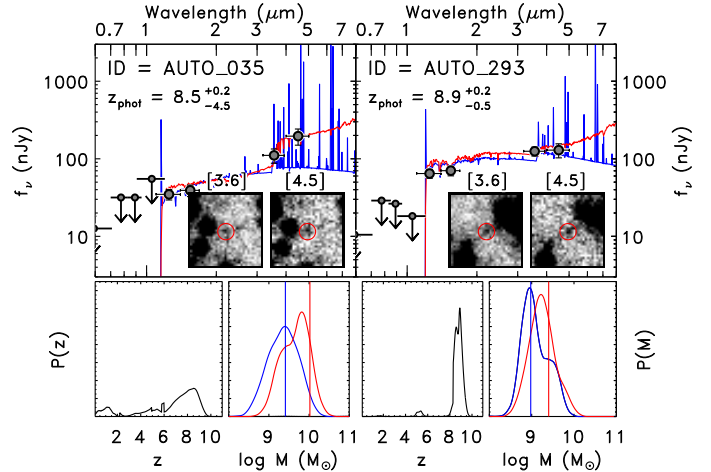


FIG. 4.— Summary of SED fitting results for AUTO_035 (left) and 293 (right). The results obtained from the fit with and without the contributions from nebular lines are coded in blue and red, respectively. The top panels show the observed SEDs (grey circles) and the best-fit templates, and the insets display their 3.6 and 4.5 μm image ($18''6 \times 18''6$). The bottom panels show the likelihood functions of z_{phot} and M_* , and the best-fit values are indicated by the vertical lines.

any systematic uncertainties from the contamination due to low- z interlopers. For ease of direct comparison to observations, surface density and apparent magnitude scales are also provided on the same figures to present these results in terms of differential number densities versus apparent J_{125} magnitudes. For comparison, we also plot the *observed* densities (i.e., before corrections for their corresponding V_{eff} values) extracted from the sample of Y10 in the HUDF09 proper and those of B11 in the HUDF09, HUDF09P1 and HUDF09P2 *after* applying the additional criteria of $Y_{105} - J_{125} \geq 0.8$ mag and $J_{125} - H_{160} \leq 0.3$ mag.

An intriguing feature that our samples reveal is that there could be an excess of bright objects at $J_{125} \lesssim 26.2$ mag with respect to any of the existing Schechter LF estimates at $z \approx 8$ in the literature would predict. The inferred number density at this bright end is even higher than the prediction from a non-evolution $z \approx 7$ LF (e.g., the one from B11). This excess is still evident with the observed counts *before* applying the incompleteness correction. The observed counts at $J_{125} \lesssim 26.2$ mag in Figure 5 comes from objects AUTO_048 and AUTO_100. Based on their photometry in J_{125} and assuming $z = 8$, they have M_{UV} of -21.54 and -21.21 , respectively. While such high luminosities have been observed in the spectroscopically confirmed $z \approx 7$ galaxies of Ono et al. (2012), they are 5 – $9 \times$ more luminous than any previously known Y_{105} -dropouts. Such an excess is unlikely due to cosmic variance, whose effect is expected to be small compared to the Poisson errors for our observed number density if we use the formalism of Trenti & Stiavelli (2008).

We note that, however, that O12 do not see such an excess, even though their sample also includes our brightest candidate AUTO_048. The main reason for this discrepancy could be that O12 use a larger volume in the calculation. They have included part of the CANDELS Wide field in the GOODS-S region, which is a major contributor to their larger volume. However, this area does not have sufficiently deep Y_{105} data to apply our selection criterion of $Y_{105} - J_{125} \geq 0.80$ mag down to

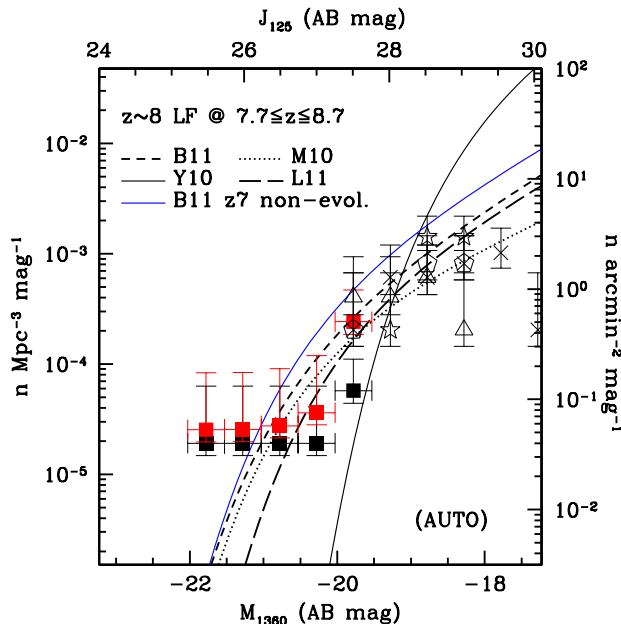


FIG. 5.— Constraints on the very bright-end of the LF at $z \approx 8$ based on the sample of Y_{105} -dropouts in CANDELS/Deep from this current work. The black squares are the differential surface densities inferred from the number counts in our sample, while the red squares are those after correction for V_{eff} with respect to the volume within $7.7 \leq z \leq 8.7$. The count predictions over $7.7 \leq z \leq 8.7$ are from the Schechter LF estimates at $z \approx 8$ from B11, M10, Y10, and L11 are shown as various black curves, together with a non-evolution one at $z \approx 7$ from B11 as the blue curve. For comparison, different symbols at the faint-end show the raw (observed) surface densities of Y_{105} -dropouts based on the following samples: Y10 (HUDF – stars), B11 (HUDF – crosses; HUDFP1 – pentagons; HUDFP2 – triangles).

$J_{125} \approx 26.0$ mag. O12 have adopted a less stringent criterion of $Y_{105} - J_{125} \geq 0.45$ mag, which allows them to construct a Y_{105} -dropout sample in this area at the cost of including candidates at lower redshifts ($z \approx 7.2$). The advantage of their approach is that they can incorporate the WFC3 ERS field in the GOODS-S region as well, which further increases their survey volume. While the WFC3 ERS field has Y_{098} but not Y_{105} data, the redshift range probed by their Y_{098} -dropouts in this area overlaps that of their Y_{105} -dropouts elsewhere, and therefore O12 has combined the Y_{098} - and the Y_{105} -dropouts to address the LF averaged over a wide redshift range ($z \approx 7-8.7$).

In contrast, our color criteria select galaxies in a higher range of redshifts, $7.7 \lesssim z \lesssim 8.7$, and the bright-end excess (with respect to a smooth Schechter function) that we find suggests that our understanding of the LF at $z \approx 8$ is still far from being complete. The significance of this excess is still subject to small number statistics, and we cannot rule out the possibility that one or both of our brightest objects could be interlopers at low redshifts. However, we should point out that similar bright-end excess at $z \approx 8$ has also been suggested in other studies, for example in the bright Y_{098} -dropout study in HIPPIES (Yan et al. 2011) at similar depths, in the ground-based survey of Laporte et al. (2011) at a brighter level, and in the much wider survey in Capak et al. (2011) at an even brighter limit²².

4.3. Implications for Star Formation in the Early Universe

Our $z \approx 8$ candidate galaxy samples have two very luminous objects and two high stellar mass objects. We have presented tentative evidence that the bright end of the galaxy LF at $z \approx 8$ might not follow the exponential cut-off of the Schechter function. While the stellar mass function at this redshift has not yet been determined, we have provided the first, albeit still tentative measurement at the high-mass end and shown that some galaxies with stellar masses as high as a few $\times 10^9 M_\odot$ might already in place at $z \approx 8$.

The physical origin of the exponential cut-off at the bright end of the LF or the high mass end of the MF seen at lower redshifts remains a matter of debate. At $z \sim 0$, star formation is “quenched” in halos with masses greater than $\sim 10^{12} M_\odot$ (“quenching mass”), perhaps by AGN feedback (e.g., Croton et al. 2006; Somerville et al. 2008; Gabor et al. 2011). However, at higher redshift ($z \lesssim 2$), the quenching mass may be higher (Dekel et al. 2009; Behroozi et al. 2010), and the existence of massive, rapidly star forming galaxies at $z > 2$ is well established. At $z \sim 2$, the observed exponential cut-off in the rest-frame UV LF appears to be due to dust (Reddy et al. 2010) rather than quenching. At very high redshifts, it has been noted before that the very blue rest-frame UV colors of $z \approx 7$ candidate galaxies (some of them confirmed) suggest that they may contain little dust (e.g., Oesch et al. 2010; M10; Y10; Bunker et al. 2010). Thus, at $z \approx 8$, when (1) the quenching mass is much higher than the typical halo mass, and (2) dust has little effect, perhaps we should not expect to see an exponential cutoff in the luminosity or mass functions of UV-bright galaxies.

It is interesting that the estimated stellar masses and number densities could imply a rather high efficiency of conversion of baryons into stars. For the lower stellar mass estimates, which are obtained using the models with nebular emission (the average is $\sim 2 \times 10^9 M_\odot$), and assuming that $\sim 20\%$ of the available baryons have been converted to stars, the implied halo masses are on the order of $\sim 10^{11} M_\odot$, for which the expected number density of dark matter halos in the currently favored Λ CDM cosmology is comparable to the observed number density of objects. This is consistent with the predicted star formation efficiencies and host halo masses at $z \approx 8$ from cosmological hydrodynamic simulations. However, if the true stellar masses are higher, or the star formation efficiency is lower, a rapidly growing tension arises between the number density of dark matter halos and the observed number density of galaxies (above halo mass $\sim 10^{11} M_\odot$, the halo number density declines by about two orders of magnitude for a factor of ~ 3 increase in mass). While converting 20% of the available baryons into stars may not sound excessive, this is in fact the *maximum* value that has been inferred at any epoch. Due to the presumably very low metallicity of the gas in these early objects, we might have expected much lower star formation efficiencies than are seen locally (e.g. Krumholz & Dekel 2010).

candidates in Capak et al. (2011), the true nature of these objects still remains uncertain.

²² While Bowler et al. (2012) derived different z_{ph} (~ 2) for the

5. SUMMARY

In this work, we search for candidate galaxies at $z \approx 8$ in the CANDELS Deep GOODS-S field and study their properties. Our sample of Y_{105} -dropouts hints that the number density of $z \approx 8$ galaxies at the bright-end might be higher than expected from the previous Schechter LF estimates, which lends support to the suggestion made by a number of earlier studies that there could be a bright-end excess in the galaxy number density at very high redshifts. Furthermore, two of our candidates are securely detected at 3.6 and 4.5 μm in *Spitzer* data. These are the first Y_{105} -dropouts individually detected at these wavelengths. Their derived stellar masses are on the order of $\sim 10^9 M_\odot$, from which we obtain the first measurement of the high-mass end of the galaxy stellar mass function at $z \approx 8$. If the high number densities of very luminous

and very massive galaxies at $z \approx 8$ are real, they could imply a large stellar-to-halo mass ratio and an efficient conversion of baryons to stars at very early time in the cosmic stellar mass assembly history.

We thank the referee for the useful comments, which improved the quality of this work. We also thank B. Mobasher and J. Dunlop for their comments on an earlier version of this paper. H.Y. acknowledges the support of NASA grant HST-GO-11192.1. Support for Program number HST-GO-12060 was provided by NASA through a grant from the Space Telescope Science Institute, which is operated by the Association of Universities for Research in Astronomy, Incorporated, under NASA contract NAS5-26555.

REFERENCES

- Anderson, J. & Bedin, L. R. 2010, *PASP*, 122, 1035
- Beckwith, S. V. W., Stiavelli, M., Koekemoer, A. M., et al. 2006, *AJ*, 132, 1729
- Behroozi, P. S., Conroy, C. & Wechsler, R. H. 2010, *ApJ*, 717, 379
- Bertin, E. & Arnouts, S. 1996, *A&A*, 117, 393
- Bouwens, R. J., Illingworth, G. D., Labbé, I., et al. 2011a, *Nature*, 469, 504
- Bouwens, R. J., Illingworth, G. D., Oesch, P. A., et al. 2010, *ApJ*, 709, L133 (B10)
- Bouwens, R. J., Illingworth, G. D., Oesch, P. A., et al. 2011b, *ApJ*, 737, 90 (B11)
- Bowler, R. A. A.; Dunlop, J. S.; McLure, R. J.; et al. 2012, *MNRAS*, 426, 2772
- Bradley, L. D., Bouwens, R. J., Ford, H. C., et al. 2008, *ApJ*, 678, 647
- Bradley, L. D., Bouwens, R. J., Zitrin, A., et al. 2012, *ApJ*, 747, 3
- Brammer, G. B., van Dokkum, P. G., & Coppi, P. 2008, *ApJ*, 686, 1503
- Bruzual, G. & Charlot, S. 2003, *MNRAS*, 344, 1000
- Bunker, A. J., Wilkins, S., Ellis, R. S., et al. 2010, *MNRAS*, 409, 855
- Calzetti, D. 2001, *PASP*, 113, 1449
- Capak, P., Mobasher, B., Scoville, N. Z., et al. 2011, *ApJ*, 730, 68
- Castellano, M., Fontana, A., Paris, D., et al. 2010, *A&A*, 524, A28
- Chabrier, G. 2003, *PASP*, 115, 763
- Croton, D. J., Springel, V., White, S. D. M., et al. 2006, *MNRAS*, 365, 11
- Dekel, A., Birnboim, Y., Engel, G., et al. 2009, *Nature*, 457, 451
- Dickinson, M., Stern, D., Giavalisco, M., et al. 2004, *ApJ*, 600, L99
- Finkelstein, S. L., Papovich, C., Giavalisco, M., et al. 2010, *ApJ*, 719, 1250
- Finkelstein, S. L., Papovich, C., Salmon, B., et al. 2012, *ApJ*, 756, 164
- Gabor, J. M., Davé, R., Oppenheimer, B. D. & Finlator, K. 2011, *MNRAS*, 417, 2676
- Giavalisco, M., Ferguson, H. C., Koekemoer, A. M., et al. 2004, *ApJ*, 600, L93
- González, V., Labbé, I., Bouwens, R. J., et al. 2011, *ApJ*, 735, L34
- Grogin, N. A., Kocevski, D. D., Faber, S. M., et al. 2011, *ApJS*, 197, 35
- Hall, N., Bradač, M., Gonzalez, A. H., et al. 2012, *ApJ*, 745, 155
- Hathi, N., Mobasher, B., Capak, P., Wang, W.-H., & Ferguson, H. C. 2012, *ApJ*, 757, 43
- Hickey, S., Bunker, A., Jarvis, M. J., Chiu, K. & Bonfield, D. 2010, *MNRAS*, 404, 212
- Hsieh, B.-Q., Wang, W.-H., Yan, H., et al. 2012, *ApJ*, 749, 88
- Koekemoer, A. M., Faber, S. M., Ferguson, H. C., et al. 2011, *ApJS*, 197, 36
- Kron, R. G. 1980, *ApJS*, 43, 305
- Krumholz, M. R. & Dekel, A. 2010, *MNRAS*, 406, 112
- Labbé, I., González, V., Bouwens, R. J., et al. 2010a, *ApJ*, 708, L26
- Labbé, I., González, V., Bouwens, R. J., et al. 2010b, *ApJ*, 716, L103
- Laporte, Pelló, R., Schaerer, D., N., et al. 2011, *A&A*, 531, 74
- Leggett, S. K., Golimowski, D. A., Fan, X., et al. 2002, *ApJ*, 564, 452
- Lorenzoni, S., Bunker, A. J., Wilkins, S. M., et al. 2011, *MNRAS*, 414, 1455 (L11)
- Madau, P. 1995, *ApJ*, 441, 18
- McLure, R. J., Dunlop, J. S., Cirasuolo, M., et al. 2010, *MNRAS*, 403, 960 (M10)
- Meiksin, A. 2006, *MNRAS*, 365, 807
- Oesch, P. A., Bouwens, R. J., Carollo, C. M., et al. 2010, *ApJ*, 709, L21
- Oesch, P. A., Bouwens, R. J., Illingworth, G. D., et al. 2012, *ApJ*, 759, 135
- Ono, Y., Ouchi, M., Mobasher, B., et al. 2012, *ApJ*, 744, 83
- Ouchi, M., Mobasher, B., Shimasaku, K., et al. 2009, *ApJ*, 706, 1136
- Papovich, C., Finkelstein, S. L., Ferguson, H. C., Lotz, J. M. & Giavalisco, M. 2011, *MNRAS*, 412, 1123
- Reddy, N. A., Erb, D. K., Pettini, M., Steidel, C. C., & Shapley, A. E. 2010, *ApJ*, 712, 1070
- Richard, J., Pelló, R., Schaerer, D., Le Borgne, J.-F. & Kneib, J.-P. 2006, *A&A*, 456, 861
- Ryan, R. E., Thorman, P. A., Yan, H., et al. 2011, *ApJ*, 739, 83
- Salpeter, E. E. 1955, *ApJ*, 121, 161
- Somerville, R. S., Hopkins, P. F., Cox, T. J., Robertson, B. E. & Hernquist, L. 2008, *MNRAS*, 391, 481
- Steidel, C. C., Adelberger, K. L., Giavalisco, M., Dickinson, M. & Pettini, M. 1999, *ApJ*, 519, 1
- Steidel, C. C., Adelberger, K. L., Shapley, A. E., et al. 2003, *ApJ*, 592, 728
- Szalay, A. S., Connolly, A. J. & Szokoly, G. P., 1999, *AJ*, 117, 68
- Trenti, M., Bradley, L. D., Stiavelli, M., et al. 2011a, *ApJ*, 727, L39
- Trenti, M. & Stiavelli, M. 2008, *ApJ*, 676, 767
- Trenti, M., Bradley, L. D., Stiavelli, M., et al. 2012, *ApJ*, 746, 55
- Wilkins, S. M., Bunker, A. J., Lorenzoni, S. & Caruana, J. 2011, *MNRAS*, 411, 23
- Windhorst, R. A., Cohen, S. H., Hathi, N. P., et al. 2011, *ApJS*, 193, 27
- Wyithe, J. S. B., Yan, H., Windhorst, R. A. & Mao, S. 2011, *Nature*, 469, 181
- Xue, Y. Q., Luo, B., Brandt, W. N., et al. 2011, *ApJS*, 195, 10
- Yan, H., Dickinson, M., Eisenhardt, P. R. M., et al. 2004, *ApJ*, 616, 63
- Yan, H., Dickinson, M., Stern, D., et al., 2005, *ApJ*, 634, 109
- Yan, H., Windhorst, R. A., Hathi, N. P., et al. 2010, *Res. Astron. Astrophys.*, 10, 867 (Y10)
- Yan, H., Yan, L., Zamojski, M. A., et al. 2011, *ApJ*, 728, L22

TABLE 1
MAG_AUTO-SELECTED Y_{105} -DROPOUTS IN CANDELS GOODS-S DEEP REGION

ID	RA & DEC (J2000)	J_{125}	$Y_{105} - J_{125}$ ^a	$J_{125} - H_{160}$	[3.6] ^b	[4.5] ^b	Other ID ^c
AUTO_048	3:32:49.936 -27:48:18.101	25.65±0.07	1.1±0.2	-0.2±0.1	C	C	ISO_085; O12-2499448181
AUTO_100	3:32:41.417 -27:44:37.831	25.98±0.14	1.8±0.6	0.0±0.2	B	B	ISO_164
AUTO_212	3:32:20.965 -27:51:37.073	26.39±0.15	1.0±0.3	0.1±0.2	> 26.8	> 26.2	O12-2209751370
AUTO_293	3:32:20.981 -27:48:53.467	26.88±0.17	> 1.1	-0.4±0.3	26.16±0.13	26.12±0.22	ISO_071; O12-2209848535
AUTO_204	3:32:18.185 -27:52:45.566	27.38±0.19	0.9±0.5	0.2±0.3	> 26.7	> 26.2	O12-2181852456
AUTO_094	3:32:40.675 -27:45:11.624	27.39±0.27	0.9±0.6	0.0±0.4	C	C	
AUTO_035	3:32:34.998 -27:49:21.623	27.55±0.21	> 1.2	0.3±0.3	26.29±0.22	25.67±0.25	ISO_063; O12-2350049216

^a For the objects that are not detected in Y_{105} , their $Y_{105} - J_{125}$ limits are calculated using the $2\text{-}\sigma$ flux upper limits in Y_{105} as measured within the MAG_AUTO apertures.

^b The IRAC magnitudes are MAG_APER within $r = 1''.5$ aperture, and limits are based on $2\text{-}\sigma$ flux upper limits within the same aperture, both of which are with an aperture correction to a total flux. “B” or “C” means that the object is blended with or contaminated by foreground neighbor(s) in IRAC.

^c For the common candidates in the AUTO and the ISO samples (see appendix), their ID’s in the other set are given. In addition, if an object is also in the O12 sample, its ID in O12 is given as well.

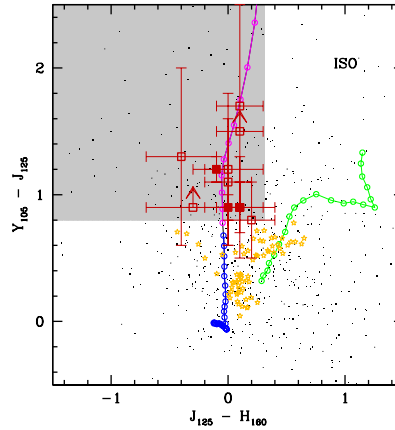


FIG. 6.— Similar to Figure 1, but for selection of Y_{105} -dropouts using MAG_ISO magnitudes.

APPENDIX

Due to the nature of the dropout selection technique, it is not unusual that samples constructed by independent groups can differ significantly on an object-by-object basis (see §3). To further demonstrate this point, we constructed a separate Y_{105} -dropout sample to mimic an independent study.

We used exactly the same data as in §2, and therefore any difference in this sample should be attributed to the selection technique. We followed the same procedures as in §3, but used MAG_ISO instead when calculating colors. The motivation of adopting MAG_ISO in this exercise is that isophotal apertures are commonly used in measuring Lyman-break galaxy colors (e.g., Steidel et al. 2003) because they often lead to higher S/N , even if they do not necessarily include all of the light from each galaxy. Hereafter we refer to this sample as the “ISO sample” to separate from the one described in the main text, which we refer to as the “AUTO sample”. The initial candidates in the ISO sample were also visually examined by the same group of six inspectors. The visual inspection of this sample was done about one month later than that for the AUTO sample, and therefore even when we were examining the same object that is also in the AUTO sample we did not keep the memory of the result from the last time, and hence we mimicked an “independent” study as much as we could.

The final ISO sample consists of eleven candidates. Fig. 6 shows their selection in the $Y_{105}J_{125}H_{160}$ color space, while Fig. 7 shows the redshift selection function. Images of these candidates are displayed in Fig. 8. Table 2 lists their photometric information.

For the sake of completeness, we also compared the ISO sample to the O12’s sample. Based on the photometry reported in O12, nine of their candidates are expected to meet our color criteria (see also §3.3.3). However, only three of them are included in our ISO sample (see Table 2). Among the five that are not in our sample, O12’s CANDY-2432246169 has $S/N < 5$ in J_{125} and H_{160} and is not included in our MAG_ISO catalog. CANDY-2272447364 has $S/N > 2$ in V_{606} and does not satisfy our optical non-detection criterion. CANDY-2277945141 and 2320345371 have $Y_{105} - J_{125} = 0.74$ and 0.57 mag based on our photometry and hence do not meet our color criteria. The other two, O12’s CANDY-2209751370 and 2181852456, meet all our color criteria, but were rejected during the visual inspection when constructing our ISO sample. Note that these latter two objects actually are in our AUTO sample (AUTO_212 and 204, respectively) and survived the visual inspection for our AUTO sample (see below).

A more constructive comparison is that between this ISO sample and the AUTO sample, which shows that they

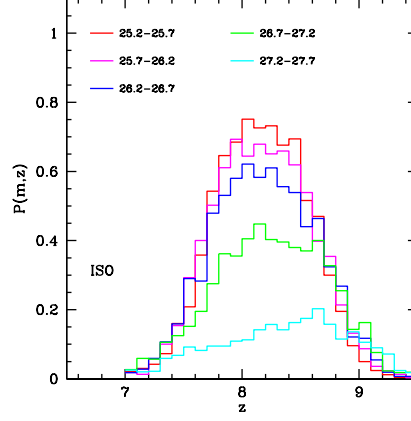


FIG. 7.— Similar to Figure 2, but for the ISO Y_{105} -dropout sample. The labeled magnitude ranges are still based on **MAG_AUTO** in J_{125} , as the simulation only has control over the input total magnitudes, which are best represented by **MAG_AUTO**. To be consistent, the correction of $V_{eff}(m)$ for the ISO sample is done at the corresponding **MAG_AUTO** ranges.

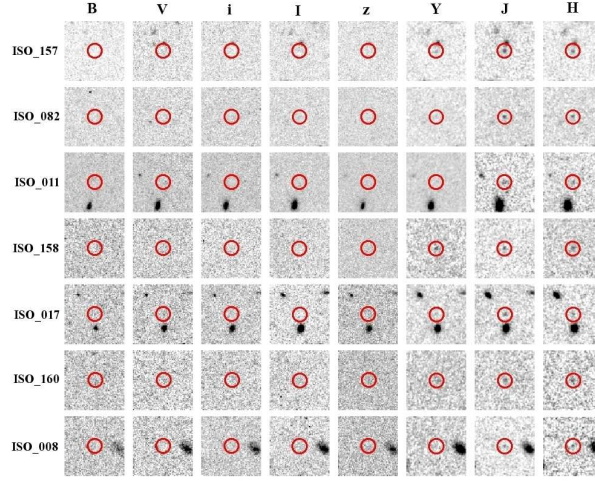


FIG. 8.— Similar to Fig. 2, but for the ISO sample. The ones that are in common with the AUTO sample are not displayed here.

have four objects in common (see Table 2). There are seven ISO candidates not in the AUTO sample. Five of them were rejected in the AUTO selection because they have $S/N > 2$ within their **MAG_AUTO** apertures in at least one veto image (ISO_011, 017, 157, 158, 160). One was rejected because its **MAG_AUTO** $Y - J$ color limit does not satisfy $Y - J > 0.8$ mag (ISO_008). The other one (ISO_082) satisfies all the quantitative criteria in the AUTO selection, however it was rejected in the visual inspection step during the AUTO selection run.

On the other hand, four AUTO candidates are not in the ISO sample. Two of them were rejected because they have **MAG_AUTO** $Y - J$ color or limit below the $Y - J > 0.8$ mag threshold (AUTO_094 and 368). The other two satisfy all the quantitative criteria in the ISO selection, however they were rejected in the visual inspection step during the ISO selection run (AUTO_204 and 212).

This internal comparison of our two samples thus further demonstrates the points addressed earlier: (1) adoption of different photometry result in samples that can be significantly different on an object-by-object basis, and (2) visual inspections at different time, especially the inspections of the veto images, can also result in differences in this sense because such inspections are not guaranteed to be fully repeatable for a large sample at the $S/N < 2$ level.

Nevertheless, the main statistical trends revealed by the ISO sample are very similar to those inferred from the AUTO sample. Both samples include the same two bright Y_{105} -dropouts (AUTO_048/ISO_085 and AUTO_100/ISO_184), and the same two IRAC-detected ones (AUTO_293/ISO_071 and AUTO_035/ISO_063). For completeness, Fig. 9 shows the constraint from the ISO sample on the LF, where one can see that the bright-end excess is still present. Similarly, the constraints on the MF and the stellar mass density derived from the ISO sample agree with those based the AUTO sample to within $\lesssim 10\%$, and the small differences are mainly caused by the slightly different V_{eff} corrections over the range of interest. From this exercise, we believe that the main results presents in this work are robust.

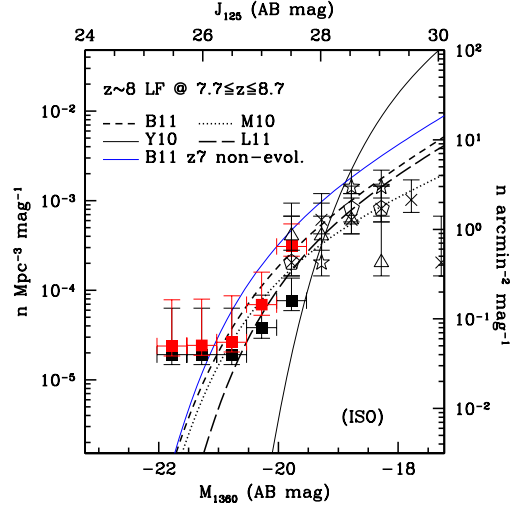


FIG. 9.— Same as Figure 5, but for the ISO sample. Note that the J_{125} magnitudes shown here are the `MAG_AUTO` magnitudes, because these are taken as the total magnitudes.

TABLE 2
MAG_ISO-SELECTED Y_{105} -DROPOUTS IN CANDELS GOODS-S DEEP REGION

ID	RA & DEC (J2000)	J_{125} ^a	$Y_{105} - J_{125}$ ^b	$J_{125} - H_{160}$ ^c	[3.6] ^d	[4.5] ^d	Other ID ^e
ISO_085	3:32:49.936 -27:48:18.100	25.65±0.07	1.2±0.1	-0.1±0.1	C	C	AUTO_048; O12-2499448181
ISO_164	3:32:41.417 -27:44:37.831	25.98±0.14	0.9±0.1	0.0±0.1	C	C	AUTO_100
ISO_157	3:32:42.882 -27:45:04.268	26.50±0.13	0.9±0.2	0.1±0.2	B	B	
ISO_071	3:32:20.981 -27:48:53.468	26.88±0.17	1.7±0.8	0.1±0.2	26.16±0.13	26.12±0.22	AUTO_293; O12-2209848535
ISO_082	3:32:14.133 -27:48:28.911	27.16±0.19	1.1±0.5	0.0±0.2	> 27.1	> 26.5	
ISO_011	3:32:14.469 -27:51:48.542	27.24±0.30	1.2±0.6	0.0±0.3	B	B	
ISO_158	3:32:47.953 -27:44:50.436	27.28±0.23	0.8±0.3	0.2±0.2	> 26.7	> 25.9	
ISO_063	3:32:34.999 -27:49:21.622	27.55±0.21	> 1.5	0.1±0.2	26.29±0.22	25.67±0.25	AUTO_035; O12-2350049216
ISO_017	3:32:18.091 -27:51:18.492	27.57±0.18	1.3±0.7	-0.4±0.3	B	B	
ISO_160	3:32:46.111 -27:44:47.997	27.88±0.50	0.9±0.4	0.1±0.3	> 26.7	> 26.1	
ISO_008	3:32:16.915 -27:52:01.878	28.00±0.27	> 0.9	-0.3±0.4	> 26.7	> 26.2	

^a. The quoted total magnitudes in J_{125} are their `MAG_AUTO` values.

^b. The $Y_{105} - J_{125}$ colors are based on their `MAG_ISO` magnitudes. For the objects that are not detected in Y_{105} , their $Y_{105} - J_{125}$ limits are calculated using the 2- σ flux upper limits in Y_{105} as measured within the `MAG_ISO` apertures.

^c. The $J_{125} - H_{160}$ colors are based on their `MAG_ISO` magnitudes.

^d. The IRAC magnitudes are `MAG_APER` within $r = 1''.5$ aperture, and limits are based on 2- σ flux upper limits within the same aperture, both of which are with an aperture correction to a total flux. “B” or “C” means that the object is blended with or contaminated by foreground neighbor(s) in IRAC.

^e. For the common candidates in the AUTO and the ISO samples, their ID’s in the other set are given. In addition, if an object is also in the O12 sample, its ID in O12 is given as well.